IOP Publishing Phys. Med. Biol. 65 (2020) 025013 (12pp) https://doi.org/10.1088/1361-6560/ab5fff

Physics in Medicine & Biology

IPEM Institute of Physics and Engineering in Medicine

PAPER

A novel computed tomography image synthesis method for correcting the spectrum dependence of CT numbers

Yi-Wen Chen[1,2], Hsin-Yuan Fang[1,3], Yi-Chun Wang[4], Shin-Lei Peng[5] and Cheng-Ting Shih[6,7,8,9]

[1] 3D Printing Medical Research Center, China Medical University Hospital, China Medical University, 40402, Taichung, Taiwan
[2] Graduate Institute of Biomedical Sciences, China Medical University, 40402, Taichung, Taiwan
[3] Department of Thoracic Surgery, China Medical University Hospital, China Medical University, 40402, Taichung, Taiwan
[4] Department of Radiology, China Medical University Hospital, China Medical University, 40402, Taichung, Taiwan
[5] Department of Biomedical Imaging and Radiological Science, China Medical University, 40402, Taichung, Taiwan
[6] Department of Medical Imaging and Radiological Sciences, Chung Shan Medical University, 40201, Taichung, Taiwan
[7] Department of Medical Imaging, Chung Shan Medical University Hospital, 40201, Taichung, Taiwan
[8] Department of Medical Imaging and Radiological Sciences, Chung Shan Medical University, No.110, Section 1, Jian-Guo North Rd., South District., Taichung 40201, Taiwan
[9] Author to whom any correspondence should be addressed.

E-mail: ctshih21@gmail.com

Keywords: computed tomography, spectrum dependence, image synthesis

RECEIVED
2 August 2019

REVISED
23 November 2019

ACCEPTED FOR PUBLICATION
9 December 2019

PUBLISHED
16 January 2020

Abstract

The quantitative evaluation of computed tomography (CT) images is widely investigated and applied in clinical diagnosis. However, the CT number of tissue can vary with scanners or applied tube voltages because of the x-ray spectrum dependence of measured linear attenuation coefficients that degrades evaluation accuracy and limits multicenter or multimodality research. This study proposed a novel CT image synthesis method to correct the spectrum dependence of CT numbers by normalizing them to the same spectrum condition. Stoichiometric calibration was performed to derive the spectrum characteristic parameters (SCPs) of six spectra from two CT scanners with different applied tube voltages. Subsequently, conversion relationships between CT numbers and tissue parameters (TPs) were determined using the SCPs and standard tissue data. The CT number of a tissue measured from a spectrum condition was converted to TPs using these relationships, and the results were used to estimate the CT number of the tissue in another spectrum condition using the corresponding SCPs. Phantom, cadaver, and patient studies were performed to evaluate the proposed method. In the phantom study, image synthesis reduced the mean difference between the CT numbers of tissue-equivalent phantoms measured using different spectra from 57.96 to 33.94 HU. In the cadaveric study, the mean difference between the CT numbers of a temporal bone flap measured using different spectra was lowered by over 57%. In the patient image study, a significant difference of 81.5 HU was observed between the mean CT numbers of femoral shafts obtained from the two scanners; this difference was reduced to less than 17 HU, which was nonsignificant, when the proposed method was used. The proposed image synthesis method could reduce the spectrum dependence of CT numbers measured with different spectra and could be applied clinically to improve the accuracy of multicenter and multimodality evaluation and research.

1. Introduction

Computed tomography (CT) has become a common tool for the clinical diagnosis of anatomical structures and diseases. The CT number (H), presented in CT images as a grayscale value, is calculated from the measured linear attenuation coefficient (μ) of tissues, which is a function of photon energy and tissue parameters (TPs), including physical density, electron density, and atomic number. Therefore, the CT number intrinsically implies the TPs and describes the elemental compositions of tissues or lesions. In addition to using visual perception, diagnosis can be performed using the quantitative evaluation of CT numbers, such as the Agatston score of atherosclerotic

disease (Agatston *et al* 1990, Shaw *et al* 2003, Greenland *et al* 2007) and characterization of urinary stone composition (Mostafavi *et al* 1998, Motley *et al* 2001, Manglaviti *et al* 2011). Furthermore, the calculation and evaluation of bone masses, bone volume fractions, and bone mineral densities based on measured CT numbers for the diagnosis of osteoporosis have been widely investigated and applied in clinical settings (Rho *et al* 1995, Schreiber *et al* 2011, 2014, Pickhardt *et al* 2013, Lee *et al* 2015). The accuracy of the evaluation is dependent on the reliability of the measured CT numbers.

However, current CT scanners employ continuous x-ray spectra to scan patients, and the measured CT numbers are calculated from the spectrum-weighted μ of tissues and water. Distinct differences can be observed between x-ray spectra generated using different imaging parameters, such as tube voltages and added filters. Even if the same imaging parameters are applied to x-ray tubes, differences in anode compositions between the tubes also result in different emitted spectra. Consequently, the same tissues can present different CT numbers between scanners; thus, the results of multicenter and multiscanner image evaluation can be inaccurate (Cropp *et al* 2013, Lamba *et al* 2014, Garner *et al* 2017). Quantitative evaluation based on CT numbers must be restricted to a single scanner to ensure consistent and comparable results.

The parametric fit model (PFM) parametrically describes the relationships among the photon energy, elemental composition, and linear attenuation coefficient of materials (Mayneord 1937, Spiers 1946). The μ of a material for a specific photon energy can be approximated using the PFM with known TPs. Further, the PFM has been modified through stoichiometric calibration to determine the relationships among the x-ray spectrum, CT number, and elemental composition of a material (Schneider *et al* 1996, 2000). After calibration, spectrum characteristic parameters (SCPs) of the x-ray spectrum can be obtained, and the CT number of a material acquired using the spectrum can be estimated using the known composition (Shih *et al* 2017). In the PFM, six fitting parameters (FPs) are introduced to adapt the change of the μ within a specific range of photon energy and atomic number. These parameters must be optimally determined for a specific range. Several FP sets have been proposed by fitting the PFM with standard cross-section data, such as the photoelectric cross-section data of substances in the energy range of 20–1000 keV used by Rutherford *et al* (1967). and the μ of hydrogen, carbon, nitrogen, oxygen, and calcium in the energy range of 20–30 keV used by Watanabe (1999). However, the abundance of elements in human tissue is not considered in the fitting of these FP sets, and the photons used in diagnostic imaging are spectral instead of monoenergetic. An FP set dedicated to the μ of the human tissues in the diagnostic x-ray spectrum remains lacking.

This study devised a novel image synthesis method to estimate the CT number under particular spectrum conditions to correct the spectrum dependence of CT numbers. Using stoichiometric calibration and standard tissue data, the SCPs of a spectrum can be calculated, and the CT number of a material acquired using the spectrum can be converted to TPs. The CT number of a material presented under other spectrum conditions can thus be estimated using the SCPs of the spectrum and TP maps. To further improve the accuracy of the PFM for approximating μ, an FP set dedicated for human tissues and the diagnostic x-ray spectrum was determined identified using mean tissue and bone composition data and reference spectra. Phantom, cadaver, and patient studies were used to test whether proposed method can accurately estimate the CT numbers of tissues in different scanning spectra and thus enable quantitative evaluation and comparison using different spectra.

2. Materials and methods

2.1. FPs for human tissues in diagnostic x-ray spectra

An FP set for the optimal approximation of the μ of human tissues in the diagnostic x-ray spectrum using the PFM was fitted. The PFM is defined by combining the cross-sections of Rayleigh scattering (RS), Compton scattering (CS), and photoelectric absorption (PE) as follows:

$$\mu(E) = \frac{c \cdot N_g \cdot Z_{\mathrm{PE}}^{a}}{E^{b}} + N_g \cdot {}_e\sigma(E) + \frac{f \cdot N_g \cdot Z_{\mathrm{RS}}^{d}}{E^{e}} \tag{1}$$

where E denotes the photon energy; N_g is the electron density in electrons/cm^3; Z_{PE} and Z_{RS} represent the effective atomic numbers ($Z_{\mathrm{eff.}}$) for PE and RS, respectively (Schneider *et al* 1996); ${}_e\sigma$ is the Klein–Nishina cross-section per electron (Attix 2004); and *a*–*f* are the FPs. The three terms in equation (1), from left to right, are the cross-sections of RS, CS, and PE, respectively. Using the cross-sections, the partial attenuation coefficients of RS, CS, and PE, respectively, can be calculated. As in equation (1), the partial attenuation coefficient of CS is independent of the atomic number and can be accurately calculated using N_g and E. However, RS and PE depend on the atomic number and photon energy, and the FPs in the cross-sections are employed to improve the approximation accuracy of the partial attenuation coefficients of RS and PE. The mean partial attenuation coefficients of the RS and PE of a material consisting of N elements can be calculated as follows:

Table 1. Elemental weight fractions of some tissues included in the calculation of mean elemental weight fractions of soft and bone tissues. Calculation results of the mean elemental weight fractions of soft and bone tissues are listed.

Element	H	C	N	O	Ca	P	Other	
Tissue	Percent of weight							ρ (g cm^{-3})
Lung-blood-filled	10.3	10.5	3.1	74.9	0.0	0.2	1.0	0.26
Adipose tissue 2	11.4	59.8	0.7	27.8	0.0	0.0	0.3	0.95
Brain-grey matter	10.7	9.5	1.8	76.7	0.0	0.3	1.0	1.04
Muscle-skeletal 2	10.2	14.3	3.4	71.0	0.0	0.2	0.9	1.05
Liver 2	10.2	13.9	3.0	71.6	0.0	0.3	1.0	1.06
Soft tissue	10.4	18.6	2.8	67.3	0.0	0.2	0.8	1.03
Skeleton-spongiosa	8.5	40.4	2.8	36.7	7.4	3.4	0.8	1.18
Sternum, male shoulder girdle	7.8	31.6	3.7	43.8	8.5	4.0	0.6	1.25
Femur (total bone)	6.3	33.3	2.9	36.2	14.3	6.6	0.4	1.42
Head-Mandible	4.6	19.9	4.1	43.5	18.7	8.6	0.6	1.68
Skeleton-cortical bone	3.4	15.5	4.2	43.5	22.5	10.3	0.6	1.92
Bone tissue	6.3	28.7	3.5	41.0	13.7	6.0	0.6	1.43

$$\bar{\mu}_{(PE,RS)}(E) = \rho N_A \sum_{i=1}^{N} \frac{w_i}{A_i} \left(\frac{(c,f) \cdot Z_{(PE,RS)}^{(a,d)+1}}{E^{(b,e)}} \right) \tag{2}$$

where N_A is Avogadro's constant, w_i and A_i denote the weight fraction and atomic mass of the ith element, ρ is the physical density of the material in g/cm^3, and Z_{PE} and Z_{RS} can be calculated using the following equation.

$$Z_{(PE,RS)} = \left[\sum \lambda_i Z_i^{(a,d)} \right]^{1/(a,d)}, \tag{3}$$

where $\lambda_i = N_g^i / N_g$. In this study, the mean elemental weight fractions of soft and bone tissues as well as reference spectra were used as weighting factors to fit the FPs using equation (2). A total of 76 tissues whose elemental compositions and physical densities were obtained from ICRU Report 46 (ICRU 1992) were included. Specifically, tissues for which the total weight fraction of H, C, N, and O was higher than 95% were classified as soft tissues. Tissues for which the total weight fraction of H, C, N, and O was lower than 95% and total weight fraction of P and Ca was higher than 3% were classified as bone tissues. The mean elemental weight fractions of the soft and bone tissues were calculated by averaging the elemental weight fractions of the 50 soft tissues with physical densities from 0.26 to 1.07 g cm^{-3} and the 26 bone tissues with physical densities from 1.18 to 1.92 g cm^{-3}, respectively. Table 1 lists the elemental weight fractions of some of the included tissues and the calculated mean elemental weight fractions of the soft and bone tissues. The mean partial attenuation coefficients of the tissue and bone at photon energies of 1–140 keV with a step of 1 keV were obtained from the National Institute of Standards and Technology (NIST) XCOM database using the mean elemental weight fractions of tissue and bone (Berger *et al* 2010). The reference spectra were generated using a tungsten anode spectral model with applied tube voltages of 80, 120, and 140 kVp and a 5 mm Al filter (Boone and Seibert 1997). The FPs were fitted by minimizing the squared differences between the weighted partial attenuation coefficients of PE an RS calculated using equation (2) and those obtained from the NIST XCOM database as follows.

$$[(a,b,c),(d,e,f)] = \arg\min \sum_{l=1}^{P} \sum_{k=1}^{O} \sum_{j=1}^{N_k} \left\{ \left[f_j^k \cdot \bar{\mu}_{(PE,RS)}^{NIST}(E_j) \right]_l - \left[f_j^k \cdot \rho N_A \sum_{i=1}^{M} \frac{w_i}{A_i} \left(\frac{(c,f) \cdot Z_{(PE,RS)}^{(a,d)+1}}{E_j^{(b,e)}} \right) \right]_l \right\}^2 \tag{4}$$

where E_j and f_j^k are the photon energy and fluence, respectively, of the jth bin in spectrum k; M is the number of composition elements in the tissue and bone; N_k is the number of energy bins in spectrum k; and O is the numbers of the reference spectra; P is 2 for the tissue and bone. Minimization of equation (4) was performed using least-squares fitting with the calculation of Z_{PE} and Z_{RS} from equation (3). The FPs for PE and RS were separately fitted. The obtained FPs were applied in the following studies.

2.2. Stoichiometric calibration and determination of CT number–TP relationships

In this study, stoichiometric calibration was performed to derive the SCPs of the spectra emitted from the x-ray tubes of CT scanners. In stoichiometric calibration, the relationship among the spectrum-weighted μ of a material m relative to water, the SCPs of a spectrum s_n, and physical density and elemental composition of material m is as follows (Schneider *et al* 1996, 2000).

$$\frac{\bar{\mu}_m}{\bar{\mu}_{H_2O}} = \frac{\rho_m}{\rho_{H_2O}} \frac{\sum_{i=1}^{N} \left(\frac{w_i}{A_i}\right)\left(Z_i + Z_i^{d+1} \cdot k_1^{s_n} + Z_i^{a+1} \cdot k_2^{s_n}\right)}{\left(\frac{w_H}{A_H}\right)\left(k_1^{s_n} + k_2^{s_n} + 1\right) + \left(\frac{w_O}{A_O}\right)\left(8^{d+1} \cdot k_1^{s_n} + 8^{a+1} \cdot k_2^{s_n} + 8\right)} \tag{5}$$

where ρ_{H_2O} and ρ_m are the densities of water and material m, respectively; w_H and w_O are the weight fractions of the hydrogen and oxygen in water, respectively; and $k_1^{s_n}$ and $k_2^{s_n}$ are the SCPs of spectrum s_n. Using the general definition of the CT number and equation (5), the SCPs of spectrum s_n can be derived using the following objective function with the known elemental composition, physical density, and measured CT numbers of tissue-equivalent materials (Gammex RMI 467, Middleton, WI, USA) (Constantinou *et al* 1992).

$$(k_1^{s_n}, k_2^{s_n}) = \arg\min \sum_{u=1}^{T} \left[\left(\frac{H_{meas.}^{s_n}}{1000} + 1\right)_u - \left(\frac{\rho}{\rho_{H_2O}} \frac{\sum_{i=1}^{N} \left(\frac{w_i}{A_i}\right)\left(Z_i + Z_i^{d+1} \cdot k_1^{s_n} + Z_i^{a+1} \cdot k_2^{s_n}\right)}{\left(\frac{w_H}{A_H}\right)\left(k_1^{s_n} + k_2^{s_n} + 1\right) + \left(\frac{w_O}{A_O}\right)\left(8^{d+1} \cdot k_1^{s_n} + 8^{a+1} \cdot k_2^{s_n} + 8\right)} \right)_u \right]^2 \tag{6}$$

where $H_{meas.}^{s_n}$ and T are the measured CT number from spectrum s_n and the number of tissue-equivalent materials, respectively. The objective function [equation (6)] was minimized using least-squares fitting. In this study, two CT scanners, denoted as Scanner 1 (GE Optima CT660, GE Medical Systems, Milwaukee, WI, USA) and Scanner 2 (Toshiba Aquilion 64, Toshiba Medical Systems, Tochigi, Japan), were used. In both scanners, three tube voltages were applied on the x-ray tubes of the scanners to generate six spectra (denoted as s_1–s_6). The SCPs of the spectra were derived using equation (6) with the tissue-equivalent materials, including lung, adipose, breast, liver, brain, bones with different bone mineral densities and water (Constantinou *et al* 1992). The tissue-equivalent materials were scanned using all spectra. For each spectrum, regions of interest (ROIs) were defined on the CT images to measure the CT numbers of the tissue-equivalent materials ($H_{meas.}^{s_n}$). After calibration, the CT numbers of the tissue-equivalent materials and water were calculated using equation (5) with the known elemental composition, physical density, and derived SCPs of each spectrum ($H_{calc.}^{s_n}$). A relationship between the measured and calculated CT numbers of the tissue-equivalent materials for each spectrum ($H_{calc.}^{s_n}$–$H_{meas.}^{s_n}$ relationship) was established to correct the CT number calculated using the elemental composition, physical density, and SCPs.

The derived SCPs were applied to determine the conversion relationships between the measured CT number and TPs for each calibrated spectrum ($H_{meas.}^{s_n}$–TP relationships). For each spectrum, the calculated CT numbers ($H_{calc.}^{s_n}$) of the standard tissue were converted into measured CT numbers ($H_{meas.}^{s_n}$) using the corresponding $H_{calc.}^{s_n}$–$H_{meas.}^{s_n}$ relationship of the tissue-equivalent materials. The conversion relationships of $H_{meas.}^{s_n}$–N_g, $H_{meas.}^{s_n}$–$N_g Z_{PE}^a$, and $H_{meas.}^{s_n}$–$N_g Z_{RS}^d$ were determined through linear fitting. To reduce fitting errors, all standard tissues were classified into lung, soft tissue, or bone groups using the $H_{meas.}^{s_n}$ of adipose tissue and connective tissue as thresholds, and piecewise linear fitting was performed for each group. Figure 1 illustrates the $H_{meas.}^{s_n}$–N_g and $H_{meas.}^{s_n}$–$N_g Z_{PE}^a$ relationships determined through linear fitting of the standard tissue data and the measured CT number converted from the CT number calculated using equation (5) with the SCPs of s_2.

2.3. Synthesis of spectrum-dependent CT numbers and evaluation

Using stoichiometric calibration and the $H_{meas.}^{s_n}$–TP conversion relationships, the spectrum used for a CT scan can be described by the SCPs, and the acquired CT number of a material can be converted into TPs. Thus, the measured CT number of the material can be decomposed into SCPs and TPs. By rewriting equation (5), the CT number of a material with TPs of m_n measured using a spectrum s_v can be estimated using the following equation.

$$H_{syn.}^{s_v,m_n} = \left\{ \frac{\left[N_g\left(1 + Z_{RS}^d \cdot k_1^{s_v} + Z_{PE}^a \cdot k_2^{s_v}\right)\right]_{m_n}}{\left[N_g\left(1 + Z_{RS}^d \cdot k_1^{s_v} + Z_{PE}^a \cdot k_2^{s_v}\right)\right]_{H_2O}} - 1 \right\} \cdot 1000 \tag{7}$$

where m_n indicates the TPs converted from the CT number of the materials m originally acquired using spectrum s_n. In this study, six calibrated spectra from the two scanners were evaluated. In addition, the TPs of the same materials converted from the CT numbers acquired using different spectra and the corresponding $H_{meas.}^{s_n}$–TP conversion relationships were considered different (m_1 to m_6) and were compared. Figure 2 illustrates the procedure of synthesis of CT images using equation (7) with the SCPs and TPs from different scanners and the comparison between the acquired and synthesized CT images. The CT number of a sample acquired using spectrum n ($H_{meas.}^{s_n}$) was converted into TPs (m_n) using the corresponding $H_{meas.}^{s_n}$–TP conversion relationships. The CT number of the sample was measured using spectrum v ($H_{meas.}^{s_v}$) and was also estimated using equation (7) with the converted TPs (m_n) and SCPs of spectrum v ($H_{syn.}^{s_v,m_n}$). The accuracy of the estimated CT number of the sample ($H_{syn.}^{s_v,m_n}$) was evaluated by calculating the difference (ΔH) between the measured and estimated CT numbers of the sample.

Phantom, cadaver, and patient imaging studies were conducted to evaluate the performance of the proposed image synthesis method. In the phantom study, CT images of the tissue-equivalent materials were acquired using six calibrated spectra (s_1–s_6). To reduce the differences between the scanning positions of the two scanners, the tissue-equivalent materials were aligned using a positioning laser placed at the center of the field of view of the

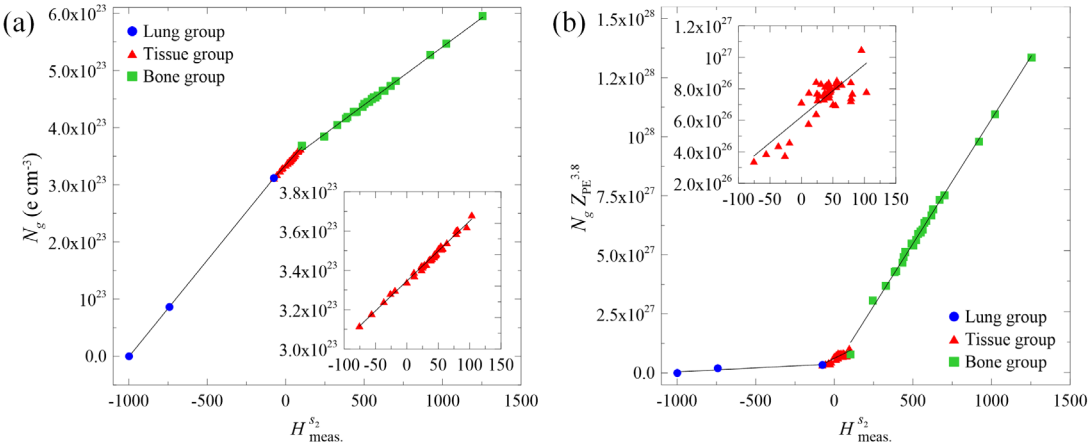

Figure 1. (a) $H^{s_n}_{meas.}$–N_g and (b) $H^{s_n}_{meas.}$–$N_g Z^a_{PE}$ relationships determined through linear fitting of standard tissue data and the measured CT number converted from the CT number calculated using equation (5) with the SCPs of s_2.

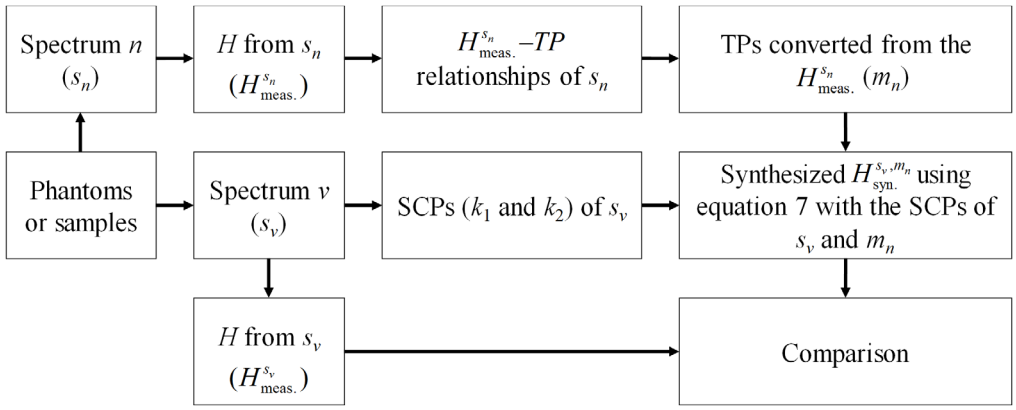

Figure 2. Procedure of CT image synthesis using equation (7) with SCPs and TPs and comparative evaluation.

scanners. The CT images were reconstructed with a slice thickness of 5 mm according to common imaging protocol for clinical abdominal CT scans and a field of view of 400 × 400 mm^2. To evaluate the performance of the image synthesis method using the same SCPs with different TP maps and the influence of the applied FPs, the CT images acquired using s_1, s_3, s_4, s_5, and s_6 were converted to TP maps of m_1, m_3, m_4, m_5, and m_6, respectively. These TP maps were further used to synthesize CT images of $H^{s_2,m_1}_{syn.}$, $H^{s_2,m_3}_{syn.}$, $H^{s_2,m_4}_{syn.}$, $H^{s_2,m_5}_{syn.}$, and $H^{s_2,m_6}_{syn.}$ using equation (7) with the SCPs of s_2 and the FPs proposed by Rutherford *et al* and Watanabe as well as those derived in this study. In addition, image synthesis using all combinations of SCPs and TP maps was performed to assess the robustness of the proposed method. For evaluation, ΔH maps between the acquired images and the CT images synthesized using SCPs identical to those of the acquired images were calculated. Circular ROIs were drawn on the ΔH maps to measure the mean and standard deviation (σ) of the ΔH values in the tissue-equivalent rods.

In the cadaveric study, CT images of a temporal bone flap were acquired using the six calibrated spectra. The bone flap was fixed in a water-filled plastic box marked with lines for positioning. The CT images were reconstructed with a slice thickness of 0.625 mm and a field of view of 400 × 400 mm^2. In contrast to those in the phantom study, the CT images in the cadaveric study were synthesized using the same TP map but different SCPs. The TP map of m_3 converted from the bone flap CT image using s_3 was used to synthesize the CT images of $H^{s_1,m_3}_{syn.}$, $H^{s_2,m_3}_{syn.}$, and $H^{s_5,m_3}_{syn.}$ using equation (7) with SCPs of s_1, s_2, and s_5. The ΔH maps between the acquired CT images and the CT images synthesized using SCPs identical to those of the acquired image and the TP maps of m_3 were calculated. The mean and standard deviation of the ΔH maps were calculated.

In the patient image study, abdominal CT images of 20 patients were retrospectively retrieved through a picture archiving and communication system with the approval of the local Institutional Review Board (No. CMUH107-REC3-087). The patients scanned by the two scanners were different. The abdominal CT images were acquired using a tube voltage of 120 kVp (s_2 and s_5) and were reconstructed with a slice thickness of 5 mm. Circular ROIs were manually defined in uniform regions of the abdominal CT images by a radiologist with 11 years of clinical experience to measure the average CT numbers of tissues, including lung, muscle, liver, and femoral shaft ($H^{s_2}_{meas.}$ and $H^{s_5}_{meas.}$). For the lung tissue, the bronchus, bronchioles, and vessels were avoided. For the

Table 2. FPs proposed by Rutherford *et al* and Watanabe as well as those derived in this study.

Parameter	Rutherford *et al*	Watanabe	Proposed
a	3.62	3.4	3.8
b	3.28	3.2	3.18
c	2.06×10^{-23}	2.30×10^{-23}	9.86×10^{-24}
d	1.86	1.5	1.75
e	2.02	1.6	1.7
f	2.80×10^{-24}	1.70×10^{-24}	2.93×10^{-24}

Table 3. Mean ratios $\pm\ \sigma$ of the mean spectrum-weighted partial attenuation coefficients of the soft and bone tissues for which the mean elemental composition was calculated using equation (2) with the FPs derived from least-squares fitting ($\bar{\mu}^{\text{calc.}}_{(PE,RS)}$) and those obtained from the NIST XCOM database ($\bar{\mu}^{\text{NIST}}_{(\text{PE,RS})}$).

	Mean $\bar{\mu}^{\text{calc.}}_{(PE,RS)}/\bar{\mu}^{\text{NIST}}_{(\text{PE,RS})}$ ratio $\pm\ \sigma$			
	Tissue		Bone	
Tube voltage (kVp)	PE	RS	PE	RS
80	0.98 ± 0.03	1.00 ± 0.06	0.98 ± 0.02	1.00 ± 0.07
120	1.01 ± 0.05	1.03 ± 0.06	0.99 ± 0.02	1.01 ± 0.03
140	1.02 ± 0.05	1.04 ± 0.07	0.99 ± 0.03	1.02 ± 0.07

muscle tissue, the ROI was drawn in the psoas muscle. For the liver, arteries and veins were avoided. For the femoral shaft, the ROI was in the cortical layer. The mean and standard deviation of the CT numbers of the tissues were calculated from the ROI-measured results of 20 patients and compared between the two scanners. Additionally, the ROI-measured CT numbers were converted to the TPs of the tissues using the corresponding conversion relationships, and the converted TPs and SCPs from the different scanners were used to estimate the CT numbers of the tissues ($H^{s_2,m_5}_{\text{syn.}}$ and $H^{s_5,m_2}_{\text{syn.}}$). The mean and standard deviation of the estimated CT numbers of the tissues were computed and compared with the mean values obtained from the ROI analysis to evaluate the performance of the proposed image synthesis method for correcting the spectral dependence of the CT number by calculating the ΔH and performing a rank sum test with statistical significance defined as a p value of less than 0.05.

3. Results and discussion

Table 2 lists the FPs proposed by Rutherford *et al* and Watanabe and those derived for the μ of the human tissues in the diagnostic x-ray spectrum in this study. Table 3 lists the mean ratios $\pm\sigma$ of the mean spectrum-weighted partial attenuation coefficients of the soft and bone tissues for which the mean elemental composition was calculated using equation (2) with the FPs derived through least-squares fitting and those obtained from the NIST XCOM database. For all spectra, the mean ratios were lower than 5%, indicating the accuracy of the derived FPs. In the least-squares fitting of the SCPs, the absolute mean errors between the measured and calculated μ of the tissue-equivalent materials relative to water was lower than 6% for all spectra. Table 4 lists the derived SCPs (k_1 and k_2) of the six calibrated spectra from the two scanners. These SCPs were used in the following synthesis of CT images.

Figure 3 presents the $H^{s_1}_{\text{meas.}}$, $H^{s_2}_{\text{meas.}}$, $H^{s_3}_{\text{meas.}}$, $H^{s_4}_{\text{meas.}}$, $H^{s_5}_{\text{meas.}}$, and $H^{s_6}_{\text{meas.}}$ images. The first row of figure 4 shows the maps of ΔH between the $H^{s_2}_{\text{meas.}}$ and $H^{s_1}_{\text{meas.}}$, $H^{s_3}_{\text{meas.}}$, $H^{s_4}_{\text{meas.}}$, $H^{s_5}_{\text{meas.}}$, and $H^{s_6}_{\text{meas.}}$ images. The ΔH values varied with the spectrum. Moreover, higher ΔH values were observed for the bone-equivalent materials than for the soft-tissue equivalents. The second through fourth rows of figure 4 present the maps of the ΔH between the $H^{s_2}_{\text{meas.}}$ and synthesized $H^{s_2,m_1}_{\text{syn.}}$, $H^{s_2,m_3}_{\text{syn.}}$, $H^{s_2,m_4}_{\text{syn.}}$, $H^{s_2,m_5}_{\text{syn.}}$, and $H^{s_2,m_6}_{\text{syn.}}$ images. For all FP sets, the ΔH values between the acquired and synthesized images for s_2 were reduced.

Figure 5 shows the ΔH values as a function of the $Z_{\text{eff.}}$ of the tissue-equivalent materials. As demonstrated in figure 5(a), the ΔH values between the images acquired using different spectra increased as the $Z_{\text{eff.}}$ increased for all spectra, indicating the dependence of CT number on the spectrum and material composition. Although the general definition of the CT number uses the μ of water as a normalizer to reduce the influence from the spectrum dependence of the CT number, the material dependence remained, and the effect of applying the μ of water as a normalizer decreased as the difference between the $Z_{\text{eff.}}$ of the tissues and water increased. Therefore, the ΔH values of the tissue-equivalent materials, which have $Z_{\text{eff.}}$ values similar to that of water, were lower than 100 HU and were similar for all spectra for tissues such as lung, adipose, breast, liver, and brain. By contrast, the ΔH values of the bone-equivalent materials, such as the inner bone, bone mineral, and cortical bone, which have $Z_{\text{eff.}}$ values higher than 10, increased as $Z_{\text{eff.}}$ increased. Figures 5(b)–(d) shows the ΔH values between the image acquired

Table 4. SCPs (denoted as k_1 and k_2) of six spectra from a GE Optima CT660 scanner with applied tube voltages of 80, 120, and 140 kVp and a Toshiba Aquilion 64 scanner with applied tube voltages of 80, 120, and 135 kVp.

Scanner		GE Optima CT660 (scanner 1)			Toshiba Aquilion 64 (scanner 2)		
Tube voltage (kVp)		80	120	140	80	120	135
Spectrum		s_1	s_2	s_3	s_4	s_5	s_6
Rutherford	k_1	-2.43×10^{-4}	-6.11×10^{-4}	-6.45×10^{-4}	3.01×10^{-4}	1.39×10^{-4}	1.9×10^{-4}
	k_2	3.56×10^{-5}	2.46×10^{-5}	1.95×10^{-5}	3.48×10^{-5}	3.02×10^{-5}	3.13×10^{-5}
Watanabe	k_1	-2.21×10^{-3}	-2.5×10^{-3}	-2.36×10^{-3}	-7.55×10^{-4}	-8.77×10^{-4}	-7.66×10^{-4}
	k_2	7.23×10^{-5}	4.9×10^{-5}	3.86×10^{-5}	7.19×10^{-5}	6.2×10^{-5}	6.44×10^{-5}
Proposed	k_1	1.84×10^{-4}	-4.48×10^{-4}	-5.62×10^{-4}	8.87×10^{-4}	6.05×10^{-4}	6.86×10^{-4}
	k_2	1.97×10^{-5}	1.35×10^{-5}	1.07×10^{-5}	1.94×10^{-5}	1.68×10^{-5}	1.75×10^{-5}

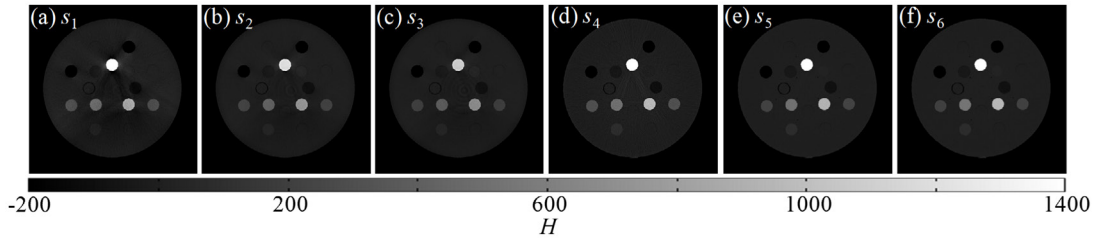

Figure 3. Phantom CT images acquired using (a) s_1, (b) s_2, (c) s_3, (d) s_4, (e) s_5, and (f) s_6.

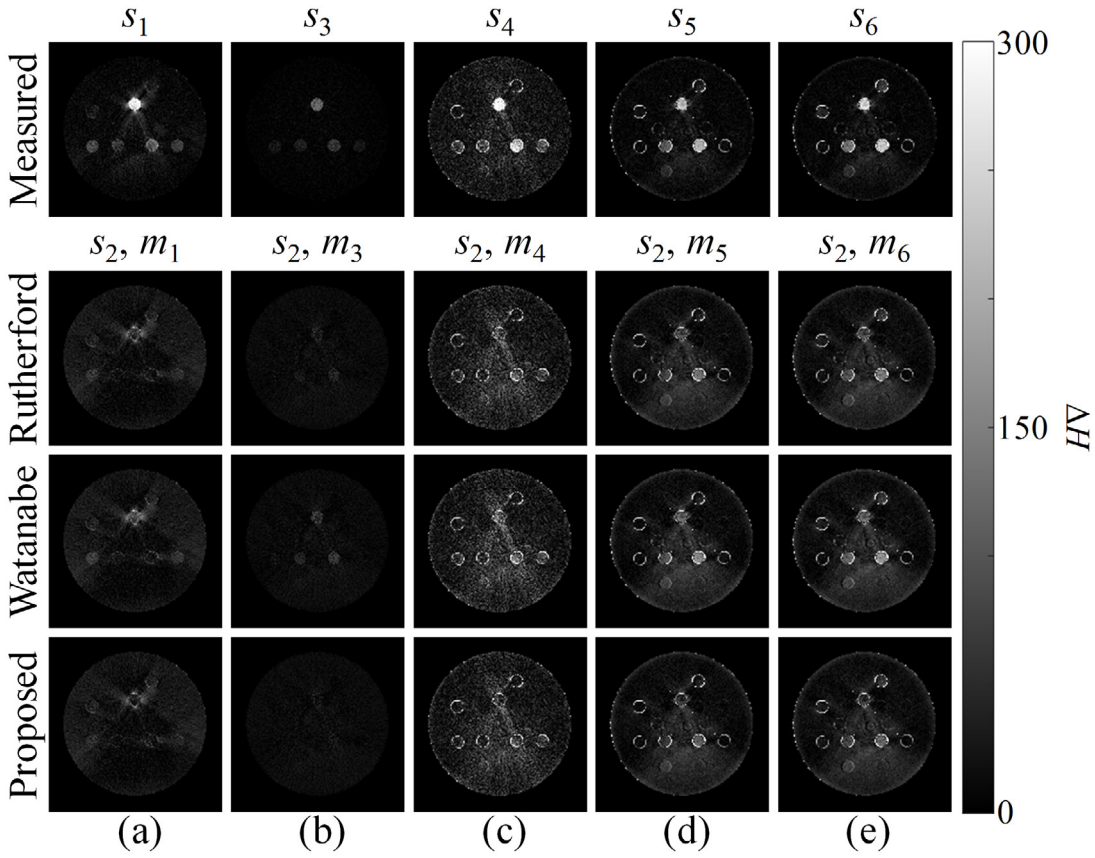

Figure 4. First row: ΔH maps between acquired images of (a) $H^{s_1}_{\text{meas.}}$, (b) $H^{s_3}_{\text{meas.}}$, (c) $H^{s_4}_{\text{meas.}}$, (d) $H^{s_5}_{\text{meas.}}$, and (e) $H^{s_6}_{\text{meas.}}$ compared with acquired image of $H^{s_2}_{\text{meas.}}$. Second through fourth rows: ΔH maps between synthesized images of (a) $H^{s_2,m_1}_{\text{syn.}}$, (b) $H^{s_2,m_3}_{\text{syn.}}$, (c) $H^{s_2,m_4}_{\text{syn.}}$, (d) $H^{s_2,m_5}_{\text{syn.}}$, and (e) $H^{s_2,m_6}_{\text{syn.}}$ using the FP sets of Rutherford *et al*, Watanabe, and this study compared with the acquired image of $H^{s_2}_{\text{meas.}}$.

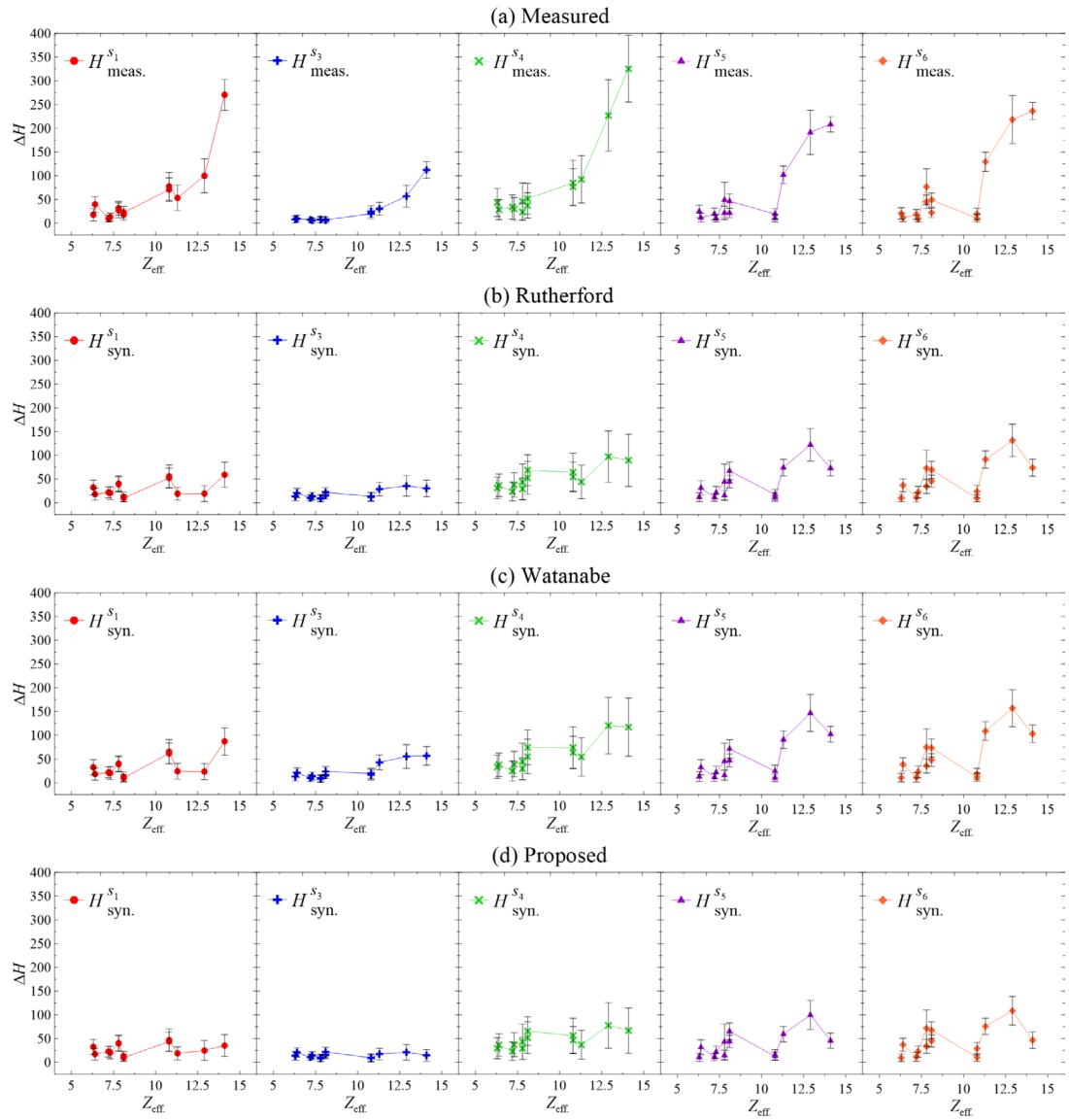

Figure 5. (a) ΔH values $\pm \sigma$ of the tissue-equivalent rods between the acquired images of $H^{s_1}_{\text{meas.}}$, $H^{s_3}_{\text{meas.}}$, $H^{s_4}_{\text{meas.}}$, $H^{s_5}_{\text{meas.}}$, and $H^{s_6}_{\text{meas.}}$ and the acquired image of $H^{s_2}_{\text{meas.}}$. ΔH values of the tissue-equivalent rods between the synthesized images of $H^{s_2,m_1}_{\text{syn.}}$, $H^{s_2,m_3}_{\text{syn.}}$, $H^{s_2,m_4}_{\text{syn.}}$, $H^{s_2,m_5}_{\text{syn.}}$, and $H^{s_2,m_6}_{\text{syn.}}$ using (b) the FP sets of Rutherford *et al*, (c) those of Watanabe, and (d) those proposed in this study and the acquired image of $H^{s_2}_{\text{meas.}}$.

using s_2 and the images synthesized using the SCPs of s_2 and applying different sets of FPs as a function of $Z_{\text{eff.}}$. For all three sets of FPs, the ΔH values of the tissue-equivalent phantoms between the acquired and synthesized images for s_2 were lower than 160 HU. Moreover, the images synthesized using the proposed FPs exhibited ΔH values below 110 HU.

Table 5 lists the mean ΔH values $\pm \sigma$ of the tissue-equivalent phantoms between the acquired image $H^{s_2}_{\text{meas.}}$ and the synthesized $H^{s_2,m_1}_{\text{syn.}}$, $H^{s_2,m_3}_{\text{syn.}}$, $H^{s_2,m_4}_{\text{syn.}}$, $H^{s_2,m_5}_{\text{syn.}}$, and $H^{s_2,m_6}_{\text{syn.}}$ images with different sets of FPs. Compared with the FPs proposed by Rutherford *et al* and Watanabe, the images synthesized using the proposed FPs presented the lowest mean ΔH values for all applied TP maps. Thus, the proposed FPs could improve the ability of the PFM to describe the μ of the human tissues in the diagnostic x-ray spectrum. The proposed FPs were applied in the following studies.

Table 6 lists the mean ΔH values $\pm \sigma$ between the phantom CT images acquired using difference spectra and between the acquired images and images synthesized using the same SCPs of the acquired images. The ΔH values of the synthesized images were lower than those of the acquired images for all SCPs and TP maps. For the average of all tissue-equivalent rods, the image synthesis reduced the mean ΔH values from 62.5 to 34.9 HU. For the cortical bone rod, the image synthesis reduced the mean ΔH values from 170.7 to 46.0 HU.

Figure 6(a) presents the acquired and synthesized images of the bone flap. The first row of figure 6(b) shows the ΔH maps between the acquired $H^{s_3}_{\text{meas.}}$ and $H^{s_1}_{\text{meas.}}$, $H^{s_2}_{\text{meas.}}$, and $H^{s_5}_{\text{meas.}}$ images. $H^{s_1}_{\text{meas.}}$ presented the highest ΔH value. The second row of figure 6(b) presents the ΔH maps of the synthesized $H^{s_1,m_3}_{\text{syn.}}$, $H^{s_2,m_3}_{\text{syn.}}$, and $H^{s_5,m_3}_{\text{syn.}}$ images

Table 5. Mean $\Delta H \pm \sigma$ of the tissue-equivalent materials between the acquired image of $H^{s_2}_{\text{meas.}}$ and synthesized images of $H^{s_2,m_1}_{\text{syn.}}$, $H^{s_2,m_3}_{\text{syn.}}$, $H^{s_2,m_4}_{\text{syn.}}$, $H^{s_2,m_5}_{\text{syn.}}$, and $H^{s_2,m_6}_{\text{syn.}}$ with the FP sets of Rutherford *et al*, those of Watanabe, and those proposed in this study.

		Mean $\Delta H \pm \sigma$ of tissue-equivalent rods			
			Synthesized using the SCPs of the s_2		
Spectrum	Material map	Measured	Rutherford	Watanabe	Proposed
s_1	m_1	57.9 ± 69.7	30.8 ± 16.9	35.2 ± 23.2	28.2 ± 12.3
s_3	m_3	23.4 ± 30.5	18.0 ± 8.8	23.8 ± 16.9	14.6 ± 4.8
s_4	m_4	84.8 ± 90.0	51.8 ± 22.7	59.2 ± 30.8	46.3 ± 16.6
s_5	m_5	56.9 ± 68.2	42.0 ± 33.7	48.7 ± 42.5	36.7 ± 26.7
s_6	m_6	66.8 ± 78.8	48.7 ± 37.0	55.0 ± 45.7	43.9 ± 30.0
Mean		58.0 ± 22.3	38.3 ± 13.9	44.4 ± 14.7	33.9 ± 12.9

Table 6. Mean $\Delta H \pm \sigma$ of tissue-equivalent rods between phantom CT images acquired using difference SCPs and between acquired images and images synthesized using SCPs identical to those of the acquired images.

		Mean $\Delta H \pm \sigma$					
Spectrum		s_1	s_2	s_3	s_4	s_5	s_6
Spectrum	s_1		57.9 ± 69.7	77.6 ± 102.4	55.1 ± 25.6	53.3 ± 23.5	61.4 ± 33.2
	s_2	57.9 ± 69.7		23.4 ± 30.5	84.8 ± 90.0	56.9 ± 68.2	66.8 ± 78.8
	s_3	77.6 ± 102.4	23.4 ± 30.5		103.1 ± 123.9	73.6 ± 101.5	81.8 ± 112.6
	s_4	55.1 ± 25.6	84.8 ± 90.0	103.1 ± 123.9		45.5 ± 29.3	48.6 ± 26.6
	s_5	53.3 ± 23.5	56.9 ± 68.2	73.6 ± 101.5	45.5 ± 29.3		47.6 ± 8.3
	s_6	61.4 ± 33.2	66.8 ± 78.8	81.8 ± 112.6	48.6 ± 26.6	47.6 ± 8.3	
TP map	m_1		28.2 ± 12.3	20.8 ± 9.9	52.5 ± 25.3	46.2 ± 32.8	51.3 ± 40.8
	m_2	34.2 ± 25.2		8.9 ± 2.8	45.1 ± 22.4	34.4 ± 21.6	39.9 ± 28.2
	m_3	33 ± 27.3	14.6 ± 4.8		43.7 ± 20.9	30.7 ± 19.1	35.3 ± 26.3
	m_4	51.9 ± 41.7	46.3 ± 16.6	27.4 ± 12.9		43.9 ± 28.7	38.4 ± 34.9
	m_5	43.2 ± 54.4	36.7 ± 26.7	21 ± 19.7	33.3 ± 35.5		41.7 ± 14.9
	m_6	57.9 ± 55.8	43.9 ± 30.0	23 ± 23.2	36.9 ± 38.1	39.1 ± 23.5	

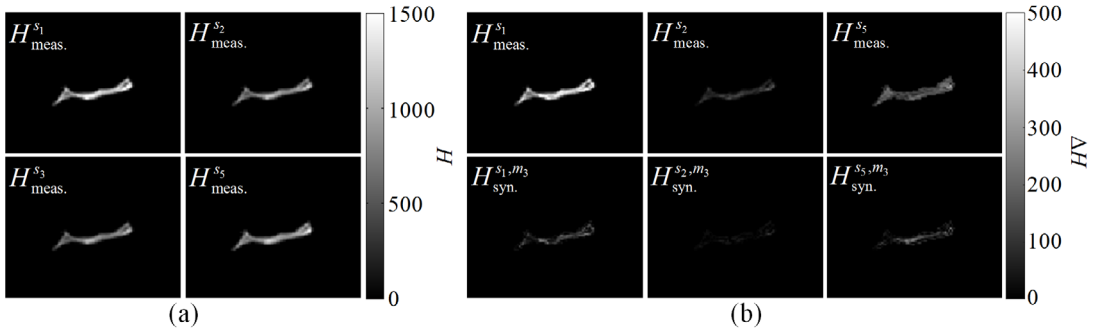

Figure 6. (a) Acquired and synthesized images of the temporal bone flap. (b) ΔH maps of the acquired and synthesized images.

and the corresponding acquired $H^{s_1}_{\text{meas.}}$, $H^{s_2}_{\text{meas.}}$, and $H^{s_5}_{\text{meas.}}$ images. The ΔH values were lower with the synthesized images.

Table 7 lists the mean ΔH values $\pm \sigma$ calculated from figure 6. Compared with the acquired images, the mean ΔH values of the synthesized images of $H^{s_1,m_3}_{\text{syn.}}$, $H^{s_2,m_3}_{\text{syn.}}$, and $H^{s_5,m_3}_{\text{syn.}}$ were 73.5%, 68.3%, and 57.2% lower, respectively. Spectrum s_1 had the lowest mean photon energy compared with spectra s_2 and s_5, and the $Z_{\text{eff.}}$ of the bone flap was higher than that of water. Therefore, the spectrum and material dependence were greatest in $H^{s_1}_{\text{meas.}}$, which exhibited the highest mean ΔH value compared with those of $H^{s_2}_{\text{meas.}}$ and $H^{s_5}_{\text{meas.}}$. Nevertheless, the low mean photon energy of spectrum s_1 also exhibited superior material differential ability compared with spectrum s_3. The TPs converted from $H^{s_1}_{\text{meas.}}$ were more accurate than those from $H^{s_5}_{\text{meas.}}$, resulting in the greatest reduction in mean ΔH value for $H^{s_1,m_3}_{\text{syn.}}$. By contrast, the reduction of the mean ΔH value for $H^{s_5,m_3}_{\text{syn.}}$ was approximately 50%. The positioning errors of the bone flap and the different rebinning processes of the scanners may have contributed to this low reduction. Conversely, spectra s_2 and s_5 were generated with a tube voltage of

Table 7. Mean $\Delta H \pm \sigma$ of the temporal bone flap calculated from figure 6.

	Mean $\Delta H \pm \sigma$ of the temporal bone flap	
Spectrum	Measured	Synthesized using the TP map of the m_3
s_1	245.3 ± 162.23	65.0 ± 56.5
s_2	56.2 ± 41.5	17.8 ± 15.3
s_5	145.8 ± 45.6	62.4 ± 57.3

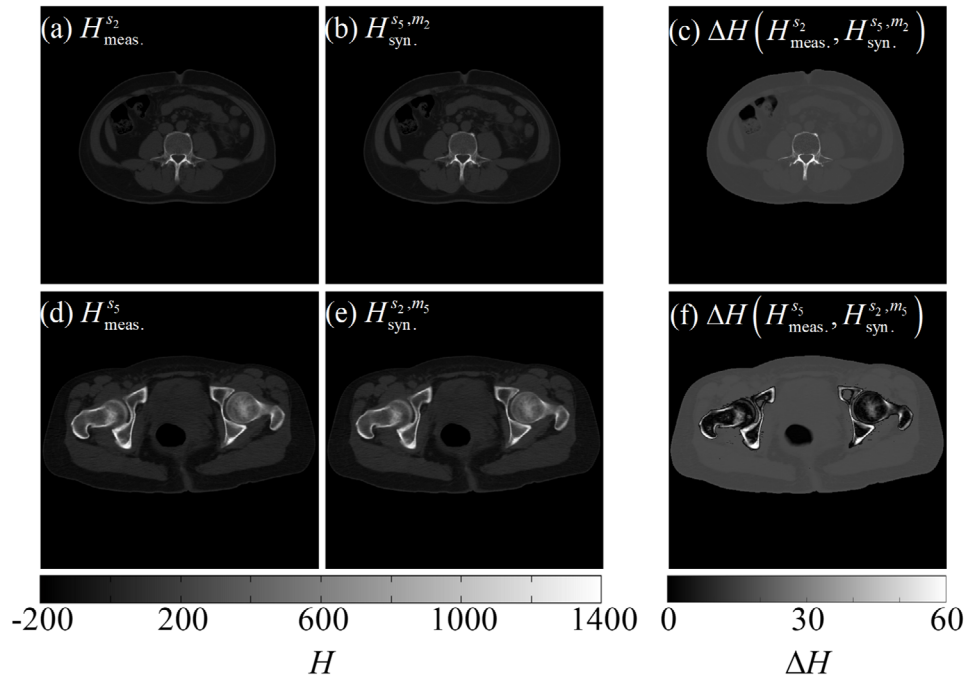

Figure 7. First row: (a) $H^{s_2}_{\text{meas.}}$ and (b) $H^{s_5,m_2}_{\text{syn.}}$ images of the abdomen and (c) ΔH maps between the images. Second row: (d) $H^{s_5}_{\text{meas.}}$ and (e) $H^{s_2,m_5}_{\text{syn.}}$ images of the pelvis and (f) ΔH maps between the images.

Table 8. Mean $\Delta H \pm \sigma$ of lung, muscle, liver, and femoral shaft tissues between the acquired and synthesized images. The p values derived from the Wilcoxon test for comparing the measured and synthesized H are presented.

	Mean $\Delta H \pm \sigma$ (p value)			
Comparison	Lung	Muscle	Liver	Femoral shaft
$H^{s_2}_{meas.}, H^{s_5}_{meas.}$	22.7 ± 53.5 (0.25)	5.1 ± 8.0 (<0.05)	5.1 ± 7.9 (0.09)	81.5 ± 65.1 (<0.01)
$H^{s_2}_{meas.}, H^{s_2,m_5}_{syn.}$	20.7 ± 54.0 (0.25)	7.9 ± 7.9 (0.36)	2.7 ± 8.0 (0.17)	16.4 ± 64.7 (0.39)
$H^{s_5}_{meas.}, H^{s_5,m_2}_{syn.}$	25.7 ± 53.9 (0.12)	4.4 ± 7.9 (0.28)	5.9 ± 8.0 (0.11)	3.7 ± 68.4 (0.91)

120 kVp and therefore presented similar $H_{\text{meas.}}$ values in the acquired images. Nevertheless, the image synthesis could further lower the difference between $H^{s_2}_{\text{meas.}}$ and $H^{s_5}_{\text{meas.}}$, and the mean ΔH value for $H^{s_2,m_3}_{\text{syn.}}$ was reduced to less than 20 HU.

The first row of figure 7 displays the $H^{s_2}_{\text{meas.}}$ and $H^{s_5,m_2}_{\text{syn.}}$ images of the abdomen and the ΔH maps between the images. The CT numbers of the $H^{s_2}_{\text{meas.}}$ and $H^{s_5,m_2}_{\text{syn.}}$ images of the soft tissue region were similar with the ΔH values being lower than 20 HU. By contrast, relatively high ΔH values reaching more than 50 HU were observed in the lumbar spine. Similar results were observed in the $H^{s_5}_{\text{meas.}}$ and $H^{s_2,m_5}_{\text{syn.}}$ images of the pelvis, as presented in the second row of figure 7. ΔH values in the hip joint, particularly in the cortical bone layer of the ischium and femoral head and neck, were higher than 60 HU. These results indicate that the image synthesis method mainly influenced the CT number of tissues with $Z_{\text{eff.}}$ values higher than that of water.

The mean ΔH values $\pm \sigma$ of the lung, muscle, liver, and femoral shaft tissues between the acquired and synthesized images are listed in table 8. The mean ΔH values between the $H^{s_2}_{\text{meas.}}$ and $H^{s_5}_{\text{meas.}}$ of all tissues were lower than 23 HU, except for the femoral shaft (81.5 HU). No significant differences were noted between the $H^{s_2}_{\text{meas.}}$ and $H^{s_5}_{\text{meas.}}$ of the lung and liver, but significant differences were observed between those of the muscle and femoral shaft. By contrast, the mean ΔH values of all tissues were below 26 HU, and no significant differences were

observed between $H_{meas.}$ and $H_{syn.}$; therefore, the proposed image synthesis method can reduce the influence of spectrum dependence on the acquired CT number without introducing additional error.

As demonstrated by the cadaveric and patient image studies, the spectrum variation from different tube voltages or scanners can influence the acquired CT numbers for tissue, especially bone tissue. The mean ΔH value of the femoral shaft between different scanners was 81.5 HU, and the mean ΔH value of the bone flap between different tube voltages was approximately 245.3 HU. If the conversion relationships between the CT number and volumetric bone mineral density are used (Lin *et al* 2017), these CT number differences can lead to errors of 6.4% to 52.4% in the converted volumetric bone mineral densities. To obtain reliable and comparable bone quality indices, the CT numbers acquired from different tube voltages or scanners must be corrected before the conversion. In contrast to previous studies, no significant differences were observed between the $H^{S_2}_{meas.}$ and $H^{S_5}_{meas.}$ of lung and liver tissues. This might be because the number of patients used in this study was insufficient to present differences in $H_{meas.}$ between scanners. The TP map used for the image synthesis was converted from the acquired CT images. As demonstrated by the phantom study, image artifacts and noise fluctuation in the acquired CT image can be propagated into the converted TP map and the subsequent synthesized CT image. Therefore, proper artifact and noise reduction methods could be applied prior to image synthesis to prevent the appearance of these undesirable image features in the synthesized image.

4. Conclusion

This study proposed an image synthesis method to correct the spectrum dependence of the CT number. Stoichiometric calibration and standard tissue data were applied to characterize the x-ray spectrum using SCPs and to determine the conversion relationship between CT number and TPs. In addition, FPs for human tissue in the diagnostic x-ray spectra were derived to improve the ability of the PFM to describe the relationship among the TPs, x-ray spectrum, and μ. The CT number of a tissue in a particular scanning spectrum can be estimated using the SCPs of the spectrum and TPs of the tissue. The CT numbers measured using different spectra can be normalized to arbitrary spectrum conditions, which can reduce the difference in the CT numbers of the same material between different tube voltages or scanners. In conclusion, the proposed image synthesis method could be applied to correct the spectrum dependence of the CT number and could assist in multimodality and multicenter image evaluation research.

Acknowledgments

The authors would like to acknowledge the support this research received from the HIWIN-CMU Joint Research and Development Center under contract HIWIN-CMU-T-106-02 and the Ministry of Science and Technology of Taiwan under contract 107-2314-B-040-028-.

Conflict of interest disclosure

The authors have no relevant conflicts of interest to disclose.

ORCID iDs

Cheng-Ting Shih https://orcid.org/0000-0002-8554-9136

References

Agatston A S, Janowitz W R, Hildner F J, Zusmer N R, Viamonte M Jr and Detrano R 1990 Quantification of coronary artery calcium using ultrafast computed tomography *J. Am. Coll. Cardiol.* **15** 827–32

Attix F H 2004 *Introduction to Radiological Physics and Radiation Dosimetry* 1st edn (New York: Wiley)

Berger M J, Hubbell J H, Seltzer S M, Chang J, Coursey J S, Sukumar R, Zucker D S and Olsen K 2010 XCOM: Photon Cross Section Database (version 1.5) (National Institute of Standards and Technology) (https://doi.org/10.18434/T48G6X)

Boone J M and Seibert J A 1997 An accurate method for computer-generating tungsten anode x-ray spectra from 30 to 140 kV *Med. Phys.* **24** 1661–70

Constantinou C, Harrington J C and DeWerd L A 1992 An electron density calibration phantom for CT-based treatment planning computers *Med. Phys.* **19** 325–7

Cropp R J, Seslija P, Tso D and Thakur Y 2013 Scanner and kVp dependence of measured CT numbers in the ACR CT phantom *J. Appl. Clin. Med. Phys.* **14** 338–49

Garner H W, Paturzo M M, Gaudier G, Pickhardt P J and Wessell D E 2017 Variation in attenuation in L1 trabecular bone at different tube voltages: caution is warranted when screening for osteoporosis with the use of opportunistic CT *Am. J. Roentgenol.* **208** 165–70

Greenland P *et al* 2007 ACCF/AHA 2007 clinical expert consensus document on coronary artery calcium scoring by computed tomography in global cardiovascular risk assessment and in evaluation of patients with chest pain: a report of the American College of Cardiology

Foundation Clinical Expert Consensus Task Force (ACCF/AHA Writing Committee to Update the 2000 Expert Consensus Document on Electron Beam Computed Tomography) developed in collaboration with the Society of Atherosclerosis Imaging and Prevention and the Society of Cardiovascular Computed Tomography *J. Am. Coll. Cardiol.* **49** 378–402

ICRU 1992 Photon, Electron, Proton and Neutron Interaction Data for Body Tissues *ICRU Report 46* (Bethesda, MD: International Commission on Radiation Units and Measurements)

Lamba R, McGahan J P, Corwin M T, Li C S, Tran T, Seibert J A and Boone J M 2014 CT Hounsfield numbers of soft tissues on unenhanced abdominal CT scans: variability between two different manufacturers' MDCT scanners *Am. J. Roentgenol.* **203** 1013–20

Lee S Y, Kwon S S, Kim H S, Yoo J H, Kim J, Kim J Y, Min B C, Moon S J and Sung K H 2015 Reliability and validity of lower extremity computed tomography as a screening tool for osteoporosis *Osteoporos. Int.* **26** 1387–94

Lin H H, Peng S L, Wu J, Shih T Y, Chuang K S and Shih C T 2017 A novel two-compartment model for calculating bone volume fractions and bone mineral densities from computed tomography images *IEEE Trans. Med. Imaging.* **36** 1094–105

Manglaviti G, Tresoldi S and Guerrer C S 2011 *In vivo* evaluation of the chemical composition of urinary stones using dual-energy CT *Am. J. Roentgenol.* **197** W76–83

Mayneord W V 1937 The significance of the Roentgen *Acta Int. Union Against Cancer* **2** 271

Mostafavi M R, Ernst R D and Saltzman B 1998 Accurate determination of chemical composition of urinary calculi by spiral computerized tomography *J. Urol.* **159** 673–75

Motley G, Dalrymple N, Keesling C, Fischer J and Harmon W 2001 Hounsfield unit density in the determination of urinary stone composition *Urology* **58** 170–3

Pickhardt P J, Pooler B D, Lauder T, del Rio A M, Bruce R J and Binkley N 2013 Opportunistic screening for osteoporosis using abdominal computed tomography scans obtained for other indications *Ann. Intern. Med.* **158** 588–95

Rho J Y, Hobatho M C and Ashman R B 1995 Relations of mechanical properties to density and CT numbers in human bone *Med. Eng. Phys.* **17** 347–55

Rutherford R A and Pullan B R, Isherwood I 1967 Measurement of effective atomic number and electron density using an EMI scanner *Neuroradiology* **11** 15–21

Schreiber J J, Anderson P A and Hsu W K 2014 Use of computed tomography for assessing bone mineral density *Neurosurg. Focus.* **37** E4

Schreiber J J, Anderson P A, Rosas H G, Buchholz A L and Au A G 2011 Hounsfield units for assessing bone mineral density and strength: a tool for osteoporosis management *J. Bone Joint Surg. Am.* **93** 1057–63

Schneider U, Pedroni E and Lomax A 1996 The calibration of CT Hounsfield units for radiotherapy treatment planning *Phys. Med. Biol.* **41** 111–24

Schneider W, Bortfeld T and Schlegel W 2000 Correlation between CT numbers and tissue parameters needed for Monte Carlo simulations of clinical dose distributions *Phys. Med. Biol.* **45** 459–78

Shaw L J, Raggi P, Schisterman E, Berman D S and Callister T Q 2003 Prognostic value of cardiac risk factors and coronary artery calcium screening for all-cause mortality *Radiology* **228** 826–33

Shih C T and Wu J 2017 Converting computed tomography images into photon interaction coefficients by using stoichiometric calibration and parametric fit models *Med. Phys.* **44** 510–21

Spiers F W 1946 Effective atomic number and energy absorption in tissues *Br. J. Radiol.* **19** 52–63

Watanabe Y 1999 Derivation of linear attenuation coefficients from CT numbers for low-energy photons *Phys. Med. Biol.* **44** 2201–11